JOURNAL OF SPACECRAFT AND ROCKETS
Vol. 31, No. 1, January–February 1994

Three-Dimensional Flow Calculations for a Projectile with Standard and Dome Bases

Jubaraj Sahu* and Charles J. Nietubicz*
U.S. Army Research Laboratory, Aberdeen Proving Ground, Maryland 21005

Test firings of the 155-mm XM825 artillery projectile have shown that its flight performance was affected by configurational changes to the base cavity. This was an unexpected result, and a clear understanding of why these changes affected the flight behavior did not exist. A computational study has been made for the two different base-cavity configurations which were flight tested. Flowfield computations have been performed at $0.8 < M < 1.5$ and $\alpha = 4.0$ deg using a recently developed three-dimensional Navier-Stokes code. The computed results show the qualitative features of the base region flowfield for the two base cavities. The base changes are found to alter the recirculation patterns in the wake, which in turn affect the expansion at the base corner. These changes in the flow structure contribute to small changes in the base pressure. Aerodynamic force and moment coefficients have been obtained from the computed pressures and are presented as a function of Mach number. Computed results show small differences in normal force and pitching moment coefficients similar to that found in the range data.

Nomenclature

a	= speed of sound
C_p	= pressure coefficient
c_0	= specific heat at constant pressure
D	= projectile diameter
e	= total energy per unit volume
$\hat{F}, \hat{G}, \hat{H}$	= flux vectors in transformed coordinates
J	= Jacobian
M	= Mach number
Pr	= Prandtl number
Pr_t	= turbulent Prandtl number
$\hat{q}$	= vector of dependent variables
R	= body radius
$\hat{S}$	= vector containing viscous terms
T	= temperature
t	= time
U, V, W	= contravariant velocities of the transformed Navier-Stokes equations
u, v, w	= axial, circumferential, and normal velocity components of the Navier-Stokes equations
x, y, z	= physical Cartesian coordinates
α	= angle of attack
γ	= ratio of specific heats
κ	= molecular and turbulent thermal conductivity
μ	= molecular and turbulent viscosity
ξ, η, ζ	= transformed coordinates
ρ	= density
ϕ	= circumferential angle
∞	= freestream conditions

Introduction

THE ability to compute the base region flowfield for projectile configurations using Navier-Stokes computational techniques has been developed over the past few years.[1-3] This capability is very important for determining aerodynamic coefficient data, including the total aerodynamic drag. The majority of base flow calculations to date have modeled the base region as a flat solid surface. Many of the actual configurations have some form of base cavity. General opinion has been that the inclusion of a base cavity or modifications to the interior cavity of a projectile base would have little or no effect on the overall flight performance parameters.

The M825 projectile, under certain conditions, is expected to be aeroballistically similar to its parent configuration, the M483A1. The M825 has an aluminum/steel base which is configured as a flat cavity (standard). A recent product improvement program (PIP), undertaken to reduce the production costs and improve shell integrity, resulted in the design of a new base configuration. This new PIP configuration has an all steel base and contains a dome cavity. A series of aeroballistic tests[4] were conducted in the Transonic Range Facility of the U.S. Army Research Laboratory (ARL) to determine any difference in the aeroballistics which may occur between the standard- and dome-base configurations. As a result of these tests, differences in aerodynamic performance were found to exist between the two rounds. The most significant changes in the aerodynamic data were in the lift and static moment coefficients. The drag was found to differ by a few percent, with the dome configuration having the lower drag at low transonic speeds.

A computational study was undertaken to determine the ability of the present Navier-Stokes codes to predict these differences and to further understand the fluid dynamic behavior which can account for such small changes. The use of Navier-Stokes codes can provide a detailed description of the flowfield associated with the M825 configuration as well as the integrated aerodynamic coefficients. The initial results for the 0-deg angle of attack case have been reported by Sahu et al.[5] This was accomplished using an axisymmetric base flow code, and the results showed the same effect as the range data; that is, a small reduction in the total aerodynamic drag at low transonic speeds ($M < 0.95$) for the dome-base configuration. The trend reversed at high transonic speeds ($M > 0.98$). This

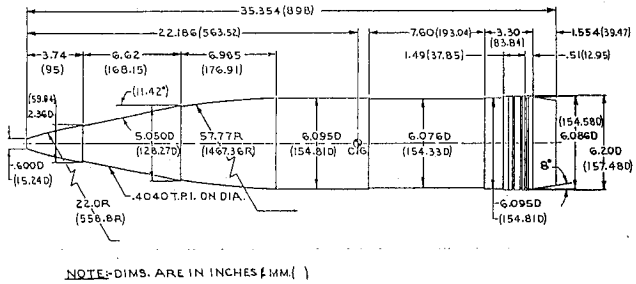

Fig. 1 M825 projectile.

Received Aug. 31, 1991; revision received March 5, 1993; accepted for publication March 5, 1993.

*Aerospace Engineer. Associate Fellow AIAA.

paper describes an extension of that work into three dimensions.

Numerical computations have been performed using a three-dimensional zonal, implicit Navier-Stokes code. The Mach number range was $0.8 < M < 1.5$ for an angle of attack $\alpha = 4.0$ deg. Results presented include the qualitative features of the base region flowfield for the two base cavities. Aerodynamic force and moment coefficients have been obtained from the computed solutions and are presented as a function of Mach number. Computed results show small differences in normal force and pitching moment coefficients similar to that found in the range data.

Governing Equations and Solution Technique

The complete set of time-dependent, thin-layer Navier-Stokes equations is solved numerically to obtain a solution to this problem. The numerical technique used is an implicit finite difference scheme. Although time-dependent calculations are made, the transient flow is not of primary interest at the present time. The steady flow, which is the desired result, is obtained in a time-asymptotic fashion.

Governing Equations

The complete set of three-dimensional, time-dependent, generalized geometry, thin-layer Navier-Stokes equations for general spatial coordinates ξ, η, and ζ can be written as[6]

$$\partial_\tau \hat{q} + \partial_\xi \hat{F} + \partial_\eta \hat{G} + \partial_\zeta \hat{H} = Re^{-1} \partial_\zeta \hat{S} \tag{1}$$

where

$\xi = \xi(x, y, z, t)$ longitudinal coordinate
$\eta = \eta(x, y, z, t)$ circumferential coordinate
$\zeta = \zeta(x, y, z, t)$ nearly normal coordinate
$\tau = t$, time

and

$$\hat{q} = \frac{1}{J}\begin{bmatrix} \rho \\ \rho u \\ \rho v \\ \rho w \\ e \end{bmatrix}, \quad \hat{F} = \frac{1}{J}\begin{bmatrix} \rho U \\ \rho u U + \xi_x p \\ \rho v U + \xi_y p \\ \rho w U + \xi_z p \\ (e+p)U - \xi_t p \end{bmatrix}$$

$$\hat{G} = \frac{1}{J}\begin{bmatrix} \rho V \\ \rho u V + \eta_x p \\ \rho v V + \eta_y p \\ \rho w V + \eta_z p \\ (e+p)V - \eta_t p \end{bmatrix}, \quad \hat{H} = \frac{1}{J}\begin{bmatrix} \rho W \\ \rho u W + \zeta_x p \\ \rho v W + \zeta_y p \\ \rho w W + \zeta_z p \\ (e+p)W - \zeta_t p \end{bmatrix} \tag{2}$$

and where

$$\hat{S} = \frac{1}{J}\begin{bmatrix} 0 \\ \mu(\zeta_x^2 + \zeta_y^2 + \zeta_z^2)u_\zeta + \frac{\mu}{3}(\zeta_x u_\zeta + \zeta_y v_\zeta + \zeta_z w_\zeta)\zeta_x \\ \mu(\zeta_x^2 + \zeta_y^2 + \zeta_z^2)v_\zeta + \frac{\mu}{3}(\zeta_x u_\zeta + \zeta_y v_\zeta + \zeta_z w_\zeta)\zeta_y \\ \mu(\zeta_x^2 + \zeta_y^2 + \zeta_z^2)w_\zeta + \frac{\mu}{3}(\zeta_x u_\zeta + \zeta_y v_\zeta + \zeta_z w_\zeta)\zeta_z \\ \left\{(\zeta_x^2 + \zeta_y^2 + \zeta_z^2)\left[\frac{\mu}{2}(u^2 + v^2 + w^2)_\zeta + \frac{\kappa a_\zeta^2}{Pr(\gamma - 1)}\right] + \frac{\mu}{3}(\zeta_x u + \zeta_y v + \zeta_z w)(\zeta_x u_\zeta + \zeta_y v_\zeta + \zeta_z w_\zeta)\right\} \end{bmatrix} \tag{3}$$

In Eq. (1), the thin-layer approximation is used, and the viscous terms involving velocity gradients in both the longitudinal and circumferential directions are neglected. The viscous terms are retained, however, for velocity gradients in a direction nearly normal to the surface where large flowfield gradients exist. These viscous terms in ζ are collected into the vector $\hat{S}$.

For this computation, the diffusion coefficients μ and κ contain molecular and turbulent parts. The turbulent contributions are supplied through an algebraic eddy-viscosity hypothesis which has been developed by Baldwin and Lomax.[7]

The velocities in the ξ, η, and ζ coordinate directions can be written as

$$U = \xi_t + u\xi_x + v\xi_y + w\xi_z$$
$$V = \eta_t + u\eta_x + v\eta_y + w\eta_z$$
$$W = \zeta_t + u\zeta_x + v\zeta_y + w\zeta_z$$

which represent the contravariant velocity components.

The Cartesian velocity components (u, v, w) are retained as the dependent variables and are nondimensionalized with respect to a_∞ (the freestream speed of sound). The local pressure is determined using the relation

$$p = (\gamma - 1)[e - 0.5\rho(u^2 + v^2 + w^2)] \tag{4}$$

where γ is the ratio of specific heats. Density ρ is referenced to ρ_∞, and the total energy e to $\rho_\infty a_\infty^2$. The transport coefficients are also nondimensionalized with respect to the corresponding freestream variables. Thus, the Prandtl number which appears in $\hat{S}$is defined as $Pr = C_{p\infty}\mu_\infty/\kappa_\infty$.

In differencing these equations, it is often advantageous to difference about a known base solution denoted by subscript zero as

$$\delta_\tau(\hat{Q} - \hat{Q}_0) + \delta_\xi(\hat{F} - \hat{F}_0) + \delta_\eta(\hat{G} - \hat{G}_0) + \delta_\zeta(\hat{H} - \hat{H}_0) - Re^{-1}\delta_\zeta(\hat{S} - \hat{S}_0) = -\partial_\tau \hat{Q}_0 - \partial_\xi \hat{F}_0 - \partial_\eta \hat{G}_0 - \partial \hat{H}_0 + Re^{-1}\partial_\zeta \hat{S}_0 \tag{5}$$

where δ indicates a general difference operator, and ∂ is the differential operator. If the base state can be properly chosen, the differenced quantities can have smaller and smoother variation and, therefore, less differencing error.

Numerical Technique

The implicit approximately factored scheme for the thin-layer Navier-Stokes equations that uses central differencing in the η and ζ directions and upwinding in ξ is written in the form

$$\left[I + h\delta_\xi^b(\hat{A}^+)^n + h\delta_\zeta \hat{C}^n - hRe^{-1}\bar{\delta}_\zeta J^{-1}\hat{M}^n J - D_i|_\zeta\right] \times [I + h\delta_\xi^f(\hat{A}^-)^n + h\delta_\eta \hat{B}^n - D_i|_\eta]\Delta\hat{Q}^n = -\Delta t\{\delta_\xi^b[(\hat{F}^+)^n - \hat{F}_\infty^+]\delta_\xi^f[(\hat{F}^-)^n - \hat{F}_\infty^-] + \delta_\eta(\hat{G}^n - \hat{G}_\infty) + \delta_\zeta(\hat{H} - \hat{H}_\infty) - Re^{-1}\bar{\delta}_\zeta(\hat{S}^n - \hat{S}_\infty)\} - D_e(\hat{Q}^n - \hat{Q}_\infty) \tag{6}$$

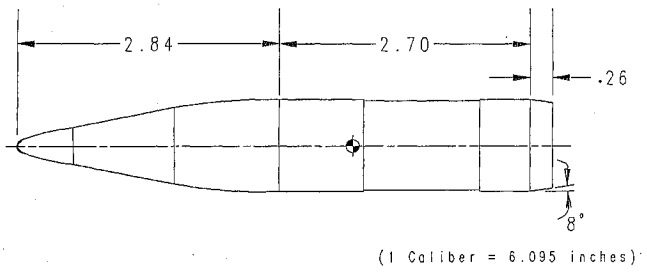

Fig. 2 Computational model.

where $h = \Delta t$ or $(\Delta t)/2$ and the freestream base solution is used. Here δ is typically a three-point second-order accurate central-difference operator, $\bar{\delta}$ is a midpoint operator used with the viscous terms, and the operators δ_ξ^b and δ_ξ^f are backward and forward three-point difference operators. The flux $\hat{F}$ has been eigensplit and the matrices $\hat{A}$, $\hat{B}$, $\hat{C}$, and $\hat{M}$ result from local linearization of the fluxes about the previous time level. Here J denotes the Jacobian of the coordinate transformation. Dissipation operators D_e and D_i are used in the central space differencing directions.

The smoothing terms used in the present study are of the form

$$D_e|_\eta = (\Delta t)J^{-1}\left[\epsilon_4\bar{\delta}\rho(B)\beta\bar{\delta} + \epsilon_4\bar{\delta}\frac{\rho(B)}{1+\beta}\bar{\delta}^3\right]|_\eta J$$

$$D_i|_\eta = (\Delta t)J^{-1}[\epsilon_4\bar{\delta}\rho(B)\beta\bar{\delta} + 2.5\epsilon_4\bar{\delta}\rho(B)\bar{\delta}]|_\eta J$$

where $\beta = |\bar{\delta}^2 p|/|(1+\delta^2)p|$ and where $\rho(B)$ is the true spectral radius of B. The idea here is that the fourth difference will be tuned down near shocks; that is, as β gets large, the weight on the fourth difference drops down whereas the second difference tunes up.

For simplicity, all of the boundary conditions have been imposed explicitly. On the body surface, the no-slip boundary condition is used and the wall temperature is specified. Freestream boundary conditions are used at the computational outer boundary. A symmetry boundary condition is imposed at the circumferential edges of the grid whereas a simple extrapolation is used at the downstream boundary. The flowfield is initially set to freestream conditions everywhere and then advanced in time until a steady-state solution is obtained. Atmospheric flight conditions were used.

Composite Grid Scheme

In the present work, a simple composite grid scheme[8] has been used where a large single grid is split into a number of smaller grids so that computations can be performed on each of these grids separately. These grids use the available core memory one grid at a time, while the remaining grids are stored on an external disk storage device such as the solid-state disk device of the Cray X-MP/48 computer. The Cray-2 has a large incore memory to fit the large single grid. However, for accurate geometric modeling of complex projectile configurations which include blunt noses, sharp corners, and base cavities, it is also desirable to split the large data base into a few smaller zones on Cray-2 as well.

The use of a composite grid scheme requires special care in storing and fetching the interface boundary data; i.e., the communication between the various zones. In the present scheme, there is a one-to-one mapping of the grid points at the interface boundaries, and thus no interpolations are required. Details of the data storage, data transfer, and other pertinent information such as metric and differencing accuracy at the interfaces can be found in Refs. 8 and 9. This scheme has been successfully used by Sahu[9] to compute three-dimensional transonic flow over two projectiles. The computed results clearly showed the transonic critical aerodynamic behavior in pitching moment coefficient observed in free flights. The present work is a further application of this technique to a more complicated projectile with base cavities.

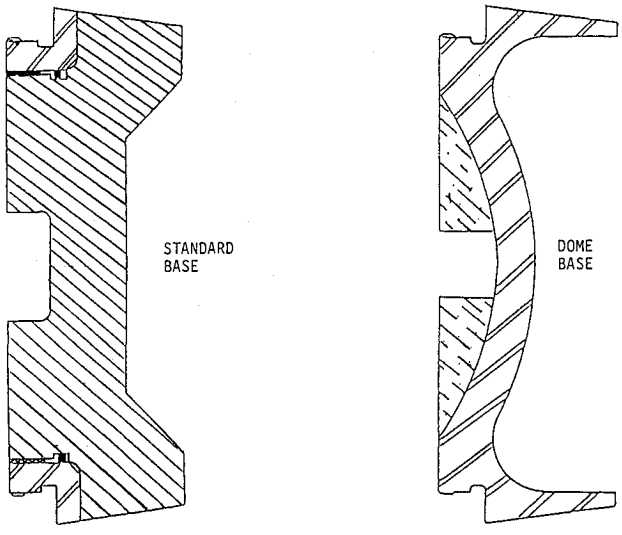

Fig. 3 Base cavity configurations.

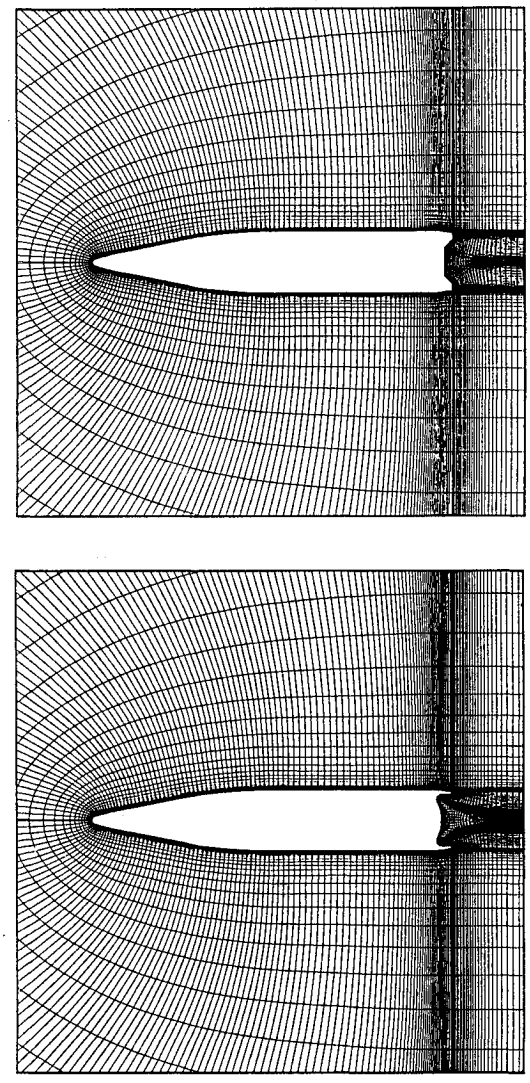

Fig. 4 Computational grid: a) standard base and b) dome base.

Model Geometry and Computational Grid

The external configuration of the M825, excluding the base, is similar to the M483A1 shown in Fig. 1. The features of this projectile, which have not been modeled exactly, are the meplat on the fuze and the rotating band near the base. The rotating band was eliminated for simplicity, and the meplat was modeled as a hemisphere cap. The computational model is shown in Fig. 2 and consists of a 2.84-caliber nose, a 2.7-caliber cylindrical section, and a 0.26-caliber 8-deg boattail. The ogive contour as well as the undercut on the cylindrical section were matched.

The current problem of interest is the effect of the different base geometries on the overall projectile aerodynamics. Figure 3 shows the standard- and dome-base configurations. The standard base is a combination of aluminum and steel and

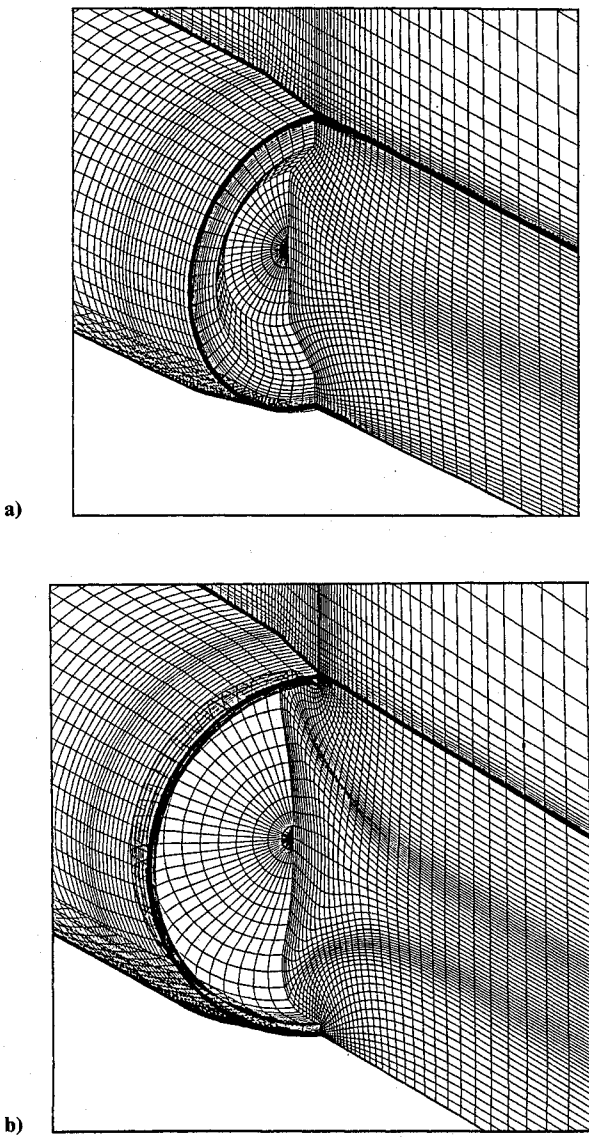

Fig. 5 Base region grid: a) standard base and b) dome base.

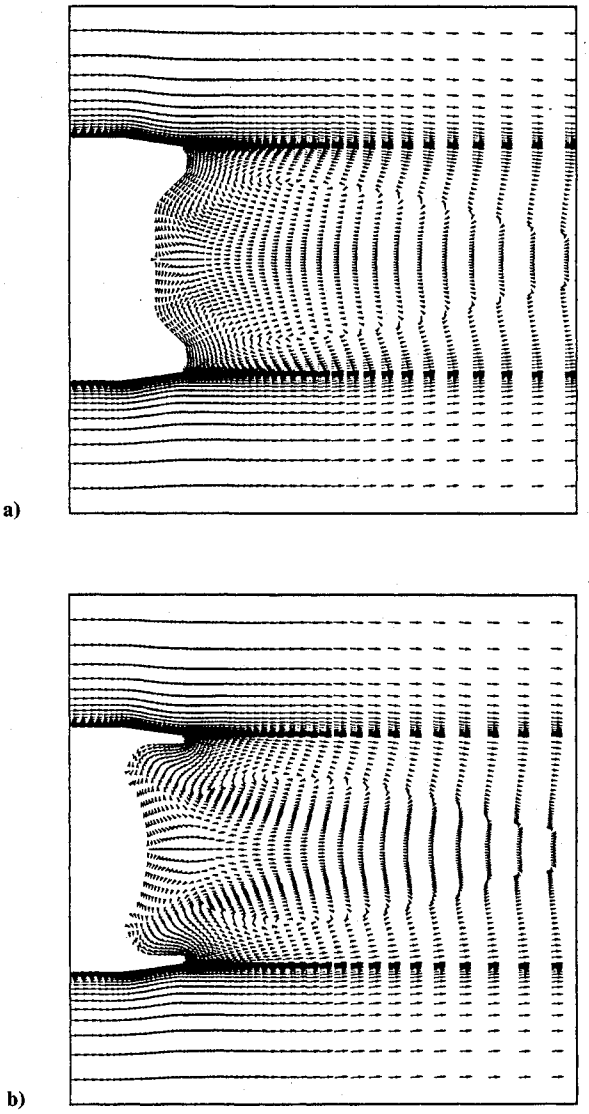

Fig. 6 Velocity vectors, $M = 0.98$, $\alpha = 0.0$ deg: a) standard base and b) dome base.

contains a base cavity which is characterized as a flat surface. The PIP configuration is an all steel base and is characterized as a dome surface. The cavity volume is also significantly larger for the dome configuration.

The solution technique requires the discretization of the entire flow region of interest into a suitable computational grid. The grid outer boundary has been placed at 2.5 body lengths upstream and surrounding the projectile. The downstream boundary was placed at 2 body lengths. Since the calculations are in the subsonic/transonic regime, the computational boundaries must extend out beyond the influence of the body. This insures that the boundary conditions specified in the flow code are satisfied.

Figures 4a and 4b show the grids generated for the standard-base and dome-base configurations, respectively. Each of these grids consists of 225 points in the streamwise direction and 50 points in the normal direction. This is broken down into two sections: a body region and a base region. The surface points for each region are selected using an interactive design program. Each grid section is then computed separately using a hyperbolic grid generation program.[10] Longitudinally, there are 106 points along the projectile surface and 60 points in the base region downstream of the base corner. The normal distribution of points in the base region consists of 50 points along the base cavity. An expanded three-dimensional view of the base grid is shown in Fig. 5a. This grid has 33 points in the circumferential direction. The generally flat sections on the standard base enabled a grid to be routinely generated. However, due to the extreme concavity of the dome configuration, this grid (Fig. 5b) required an increase in the smoothing values used by the hyperbolic grid generator, as well as the addition of a grid averaging technique.

Results

Numerical computations have been made for both the standard- and the dome-base configurations for a range of Mach numbers from $M = 0.80$ to 1.5 and at 4-deg angle of attack. Computed results obtained at 0-deg angle of attack are also included for comparison purposes.

A few qualitative results are presented next. Figures 6a and 6b show the velocity vectors in the base region for both base configurations at $M_\infty = 0.98$ and $\alpha = 0.0$ deg. The recirculatory flow in the base region is evident and as expected, is symmetric.

As shown in Fig. 6a, the recirculation region for the standard base extends to about 1.5 caliber downstream of the base corner. The back flow, on reaching the cavity, follows the contour of the cavity and leaves the cavity, pushing the flow upward. The shear layer leaving the base corner is displaced upward, weakening the expansion at the base. Figure 6b for the dome configuration shows a weak secondary bubble inside the cavity in addition to the primary bubble. The flow again

follows the contour of the cavity and, on leaving the dome cavity, is almost parallel to the streamwise direction. Thus, this flow has less effect on the free shear layer and does not weaken the expansion at the base corner as much as it does the standard base. The net effect is that the size of the primary bubble for the dome base is slightly smaller than that for the standard base. The reattachment point, therefore, is closer to the base and results in lower base pressure or higher base drag at this Mach number.[5] Figures 7a and 7b show the velocity vectors in the base region for the base configurations at $M_\infty = 0.98$ and $\alpha = 4.0$ deg for both windside (bottom half) and leeside (top half). Again, the recirculatory flow in the base region is evident and, as expected, the flow in the wake is asymmetric. As shown in these figures, the separation bubbles on windside and leeside in the wake differ in size and shape (the one on windside being thin and more elongated). In addition, a number of secondary separation bubbles can be seen to form inside the cavity for both base configurations. These changes in the flow structure contribute to small changes in the base pressure and thus, to the aerodynamic forces and moments.

Figures 8a and 8b show the Mach number contours in the base region for both base configurations at $M_\infty = 0.98$ and $\alpha = 0.0$ deg. These figures show the flow expansion at the ogive corner, boattail corner, and the base corner. One can also see a shock wave on the cylinder portion of the projectile as well as a recompression shock system which exists downstream of the base corner. The flowfield is symmetric for this condition. As angle of attack is increased to 4 deg, the flowfield becomes asymmetric (see Figs. 9a and 9b). A small asymmetry can be observed in the location of the shock wave on the cylinder. The windside shock is farther aft than the corresponding one on the leeside. The asymmetry can be clearly seen in the wake flow and its associated shock system. As can be seen in these figures, the wake flowfield changes for the different base configurations.

The entire flowfield over the projectile, including the base region, is computed. Therefore, the computed results include any upstream influence the base region flow may have on the boattail flowfield. Surface pressures, including the base pressure and the viscous stresses, are known from the computed flowfield and can be integrated to give the aerodynamic forces and moments. Comparison of the zero yaw drag coefficient is shown in Fig. 10. As seen in this figure, the difference in the computed drag is small near $M_\infty = 0.97$. The computed results show higher drag for the dome base at $1.1 < M < 1.5$ and lower drag for $M < 0.92$. Also shown on this plot is the available range data for both configurations. The overall comparison of the computed drag with the range data is fair. As seen in the range data, the dome base has a higher drag, especially at higher transonic Mach numbers, and this trend is seen in the computed results as well. Figure 11 shows the computed base pressure distribution for the dome-base configuration at $M_\infty = 1.1$ and $\alpha = 4.0$ deg for windside and leeside.

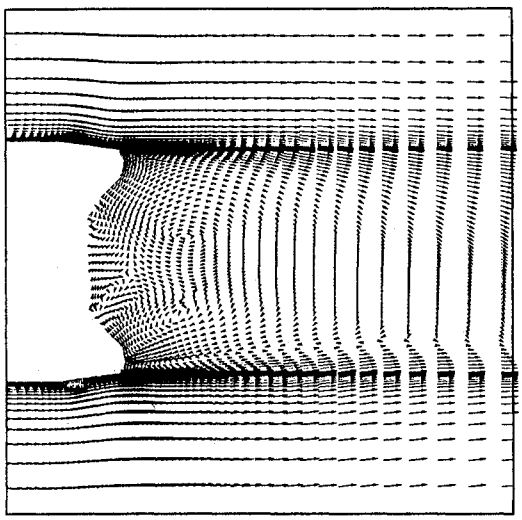

a)

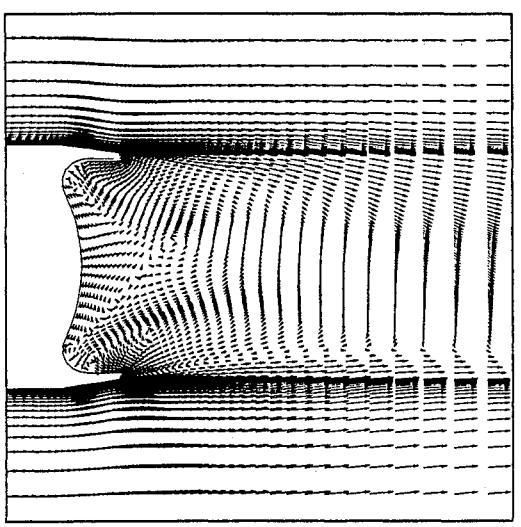

b)

Fig. 7 Velocity vectors, $M = 0.98$, $\alpha = 4.0$ deg: a) standard base and b) dome base.

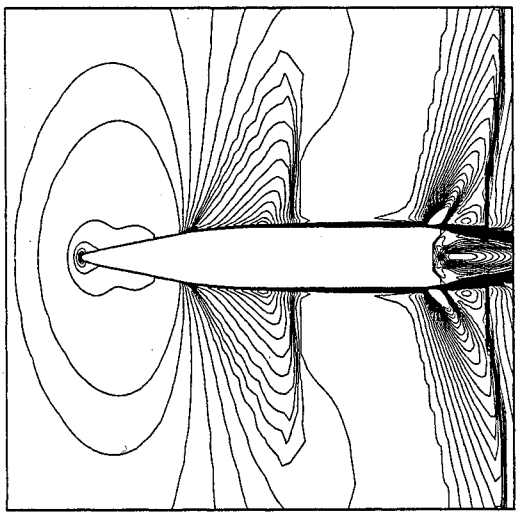

a)

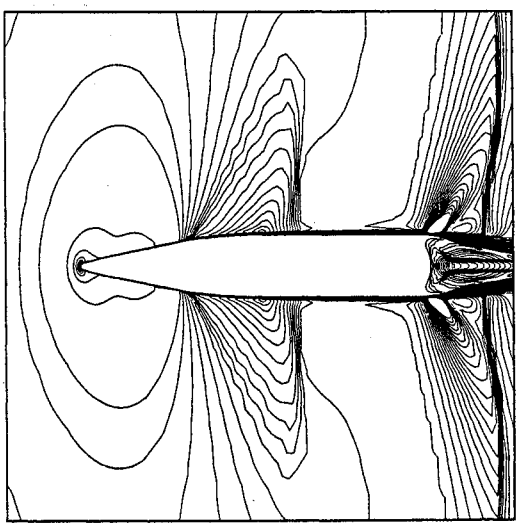

b)

Fig. 8 Mach contours, $M = 0.98$, $\alpha = 0.0$ deg: a) standard base and b) dome base.

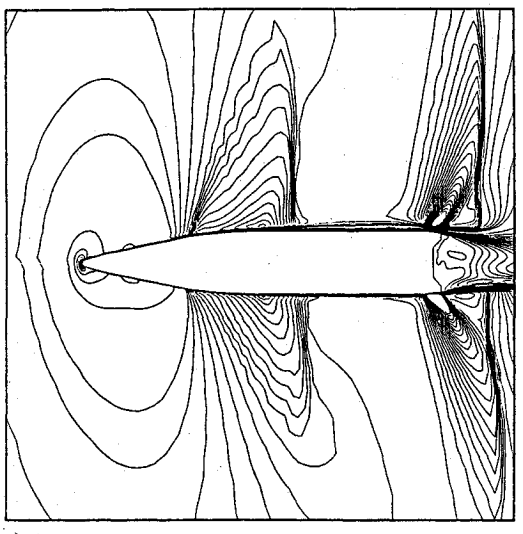

a)

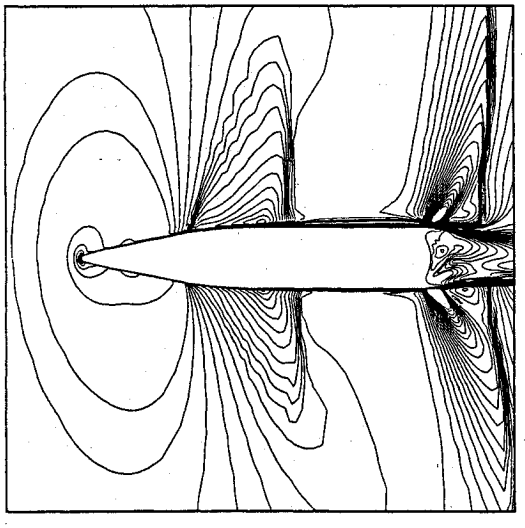

b)

Fig. 9 Mach contours, $M = 0.98$, $\alpha = 4.0$ deg: a) standard base and b) dome base.

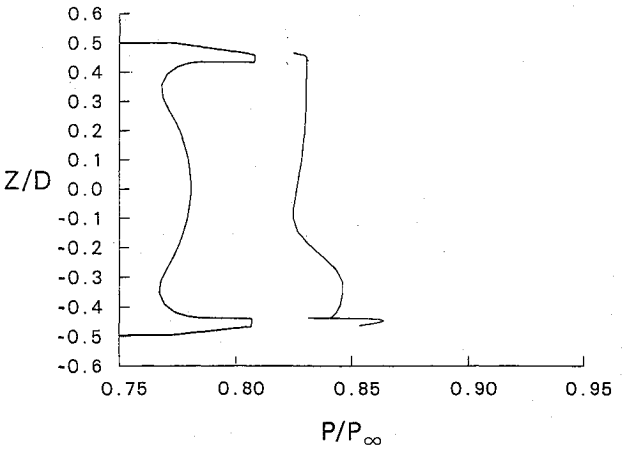

Fig. 11 Base pressure, $M = 1.1$, $\alpha = 4.0$ deg, dome base.

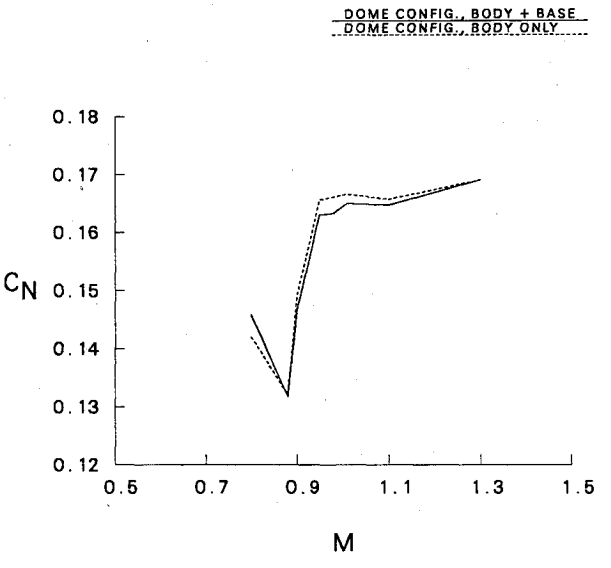

Fig. 12 Normal force vs Mach number.

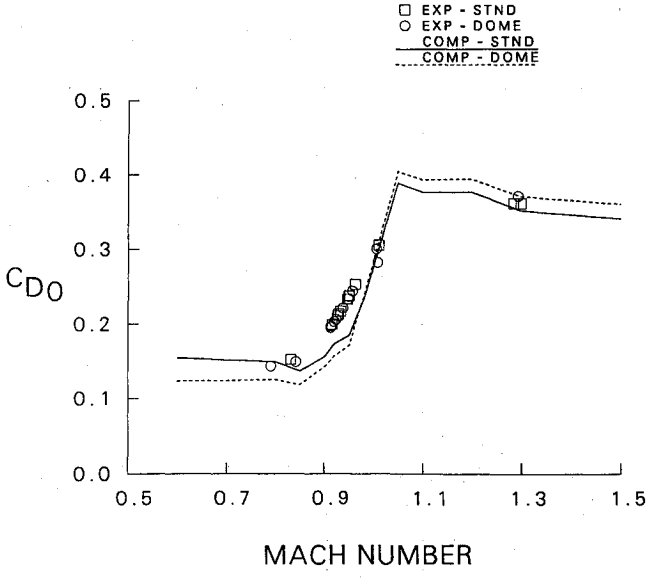

Fig. 10 Total drag vs Mach number.

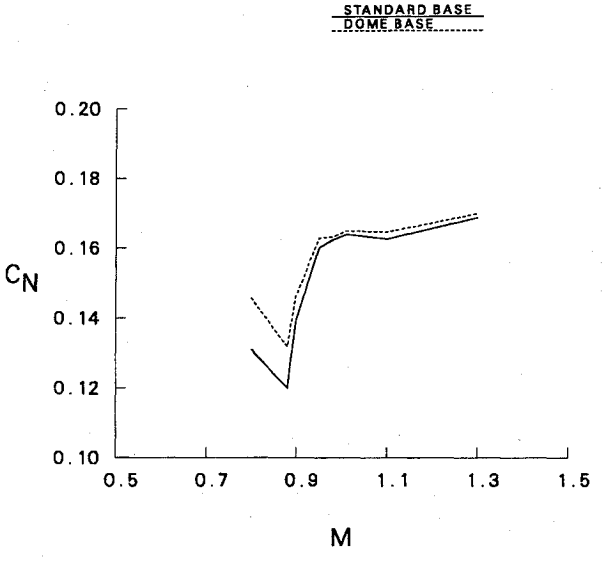

Fig. 13 C_N vs Mach number, standard base and dome base.

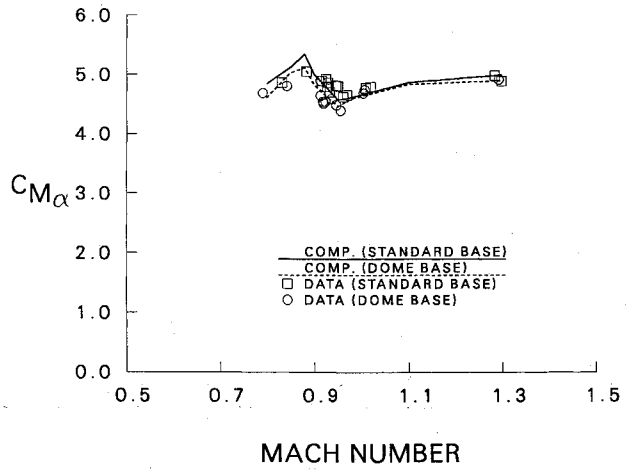

Fig. 14 Pitching moment slope, standard base and dome base.

As seen in this figure, the pressure on the windside ($Z/D = -0.5$) is higher than the pressure on leeside. Since this pressure acts normal to the inside surface of the cavity, it produces a downward force (see Fig. 12). Figure 12 shows the normal force coefficient for the dome base as a function of Mach number. The dotted line represents the normal force coefficient C_N for the dome-base projectile where the base region is excluded in the force and moment calculations. The solid line is for the entire projectile, including the contribution from the base region. As mentioned earlier, the base region produces a negative contribution, and thus, the normal force is reduced somewhat for high transonic Mach numbers ($M > 0.90$). The reverse is true for low transonic speeds ($M < 0.85$). Figure 13 shows the normal force coefficient comparison for both base configurations as a function of Mach number. The dotted line represents the dome-base result, whereas the solid line shows the result for the standard base. As seen in this figure, the dome base has a higher normal force coefficient at transonic speeds compared to the standard base. The difference is small, of the order of a few percent, at higher transonic speeds ($M > 0.90$) and gets as large as 10–12% at low transonic speeds ($M < 0.90$).

An aerodynamic coefficient which is of primary concern is the pitching moment coefficient $C_{m\alpha}$. Figure 14 shows the $C_{m\alpha}$ comparison for both base configurations. The computed $C_{m\alpha}$ is also compared with the range data[4] for both base configurations. Here, $C_{m\alpha}$ is referenced to the center of gravity of the projectile. The computed result clearly shows a sharp rise in $C_{m\alpha}$ between $M = 0.80$ and 0.88, which is followed by a sharp drop as Mach number is increased to $M = 0.95$. As the Mach number is increased further, $C_{m\alpha}$ rises gradually again, which is unlike the behavior of other projectiles, such as the M549.[9] This critical behavior in $C_{m\alpha}$ observed in the data is clearly predicted in the numerical computations. The overall comparison of the computed result with the range data is fair. As seen in the range data, the dome-base configuration has lower $C_{m\alpha}$ at transonic speeds than the standard-base configuration, and this trend is also seen in the computed results.

Conclusions

Three-dimensional numerical computations have been made for a projectile with two base-cavity configurations at transonic speeds. Computed results show differences in the qualitative features of the base-region flowfield between the two base cavities. Changes in the base-cavity configuration have been found to affect the normal force and pitching moment coefficient. Differences in these coefficients of between 0 and 12% have been predicted and are compared with the range data. The dome-base configuration produces a higher normal force and a lower pitching moment than the standard base at these transonic speeds and shows the same trend observed in the range data.

The use of computational fluid dynamics in this study has provided new insight into the fluid dynamic behavior responsible for small but important changes in the aerodynamics of the M825 projectile. This insight would have been impractical, if not impossible, to obtain through conventional testing means. The developed capability has proven to be very useful. Most importantly, it is available for design of future weapon systems and is currently being used to provide valuable design guidance in the development of an advanced multisegment projectile system.

References

[1]Sahu, J., Nietubicz, C. J., and Steger, J. L., "Navier-Stokes Computations of Projectile Base Flow With and Without Base Injection," U.S. Army Ballistic Research Lab., ARBRL-TR-02532, Aberdeen Proving Ground, MD, Nov. 1983; see also *AIAA Journal*, Vol. 23, No. 9, 1985, pp. 1348–1355.

[2]Sahu, J., "Computations of Supersonic Flow over a Missile Afterbody Containing an Exhaust Jet," *Journal of Spacecraft and Rockets*, Vol. 24, No. 5, 1987, pp. 403–410.

[3]Sahu, J., "Three-Dimensional Base Flow Calculation for a Projectile at Transonic Velocity," U.S. Army Ballistic Research Lab., BRL-MR-3610, Aberdeen Proving Ground, MD, Sept. 1987.

[4]D'Amico, W. P., Hepner, D. J., Clay, W. H., Davis, B. S., and Kendall, T. M., "Aeroballistic Testing of the M825 Projectile: Phase V—Dome Steel Base Product Improvement," U.S. Army Ballistic Research Lab., BRL-MR-3554, Aberdeen Proving Ground, MD, Dec. 1986.

[5]Sahu, J., Nietubicz, C. J., and Heavey, K. R., "Computational Study of the M825 Projectile With Standard and Dome Bases," U.S. Army Ballistic Research Lab., BRL-MR-3662, Aberdeen Proving Ground, MD, March 1988.

[6]Pulliam, T. H., and Steger, J. L., "On Implicit Finite-Difference Simulations of Three-Dimensional Flow," *AIAA Journal*, Vol. 18, No. 2, 1982, pp. 159–167.

[7]Baldwin, B. S., and Lomax, H., "Thin-Layer Approximation and Algebraic Model for Separated Turbulent Flows," AIAA Paper 78-257, Jan. 1978.

[8]Sahu, J., and Steger, J. L., "Numerical Simulation of Three-Dimensional Transonic Flows," AIAA Paper 87-2293, Aug. 1987; see also U.S. Army Ballistic Research Lab., BRL-TR-2903, Aberdeen Proving Ground, MD, March 1988.

[9]Sahu, J., "Numerical Computations of Transonic Critical Aerodynamic Behavior," AIAA Paper 88-4038, July 1988; see also U.S. Army Ballistic Research Lab., BRL-TR-2962, Aberdeen Proving Ground, MD, Dec. 1988.

[10]Nietubicz, C. J., Heavey, K. R., and Steger, J. L., "Grid Generation Technique for Projectile Configurations," *Proceedings of the 1982 Army Numerical Analysis and Computers Conference*, ARO Rept. 82-3, Aug. 1982.